Strongly Nonlinear Flow over and around a Three-Dimensional Mountain as a Function of the Horizontal Aspect Ratio

MANFRED H. BAUER, GEORG J. MAYR, IGNAZ VERGEINER, AND HELMUT PICHLER

Department of Meteorology and Geophysics, University of Innsbruck, Austria

(Manuscript received 7 December 1998, in final form 16 March 2000)

ABSTRACT

The influence of the obstacle shape, expressed through the ratio of spanwise to streamwise extension β, on flow over and around a mesoscale mountain is examined numerically. The initial wind U as well as the buoyancy frequency N are constant; the earth's rotation and surface friction are neglected. In these conditions the flow response depends primarily on the nondimensional mountain height $H_m = h_m N/U$ (where h_m is the maximum mountain height) and the horizontal aspect ratio β. A regime diagram for the onset of wave breaking, lee vortex formation, and windward stagnation is compiled. When β is increased, smaller H_m are required for the occurrence of all three features. It is demonstrated that lee vortices can form with neither wave breaking above the lee slope nor upstream stagnation. For $\beta \leq 0.5$ a vortex pair can appear although the isentropes above the lee slope do not overturn for *any* H_m. For $\beta > 1$, on the other hand, lee vortex formation is triggered by wave breaking. On the windward side two distinct processes can lead to a complete blocking of the flow: the piling up of heavier air ahead of the barrier and the upstream propagation of columnar modes, which are generated by the wave breaking process for $\beta > 1$. ''High-drag'' states and ''downslope windstorms'' exist above the threshold of wave breaking as long as no lee vortices appear (or, at least, as long as they are very small). Hence, the interval of H_m where a high-drag state occurs becomes progressively larger for larger β. With the growth of lee vortices the maximum wind speed along the leeward slope is dampened. The normalized drag drops rapidly below its linear counterpart and asymptotically approaches zero.

1. Introduction

Pioneering work in the research field of mountain airflow was done by Lyra (1940, 1943) and Queney (1948). Their analyses show stationary waves with an upstream phase tilt, which can be triggered in a vertically unbounded, stably stratified, and inviscid fluid impinging with a constant wind speed on an infinitely wide obstacle. In the succeeding decades analytical and numerical studies were primarily concerned with flow over an infinitely long barrier. The additional degree of freedom for three-dimensional flow, that is, the possibility of lateral deflection and movement around the barrier, was first determined analytically by Smith (1980) for uniform, linear flows impinging on a bell-shaped axisymmetric mountain. With increasing nondimensional mountain height $H_m = h_m N/U$ (where h_m is the maximum mountain height, N is the buoyancy frequency, and U is the initial wind speed) the flow becomes nonlinear, since the product $h_m N$ is proportional to the maximum horizontal velocity perturbation of a linear mountain-induced wave. Flow regimes for large H_m were investigated by several authors (e.g., Smith 1988; Smolarkiewicz and Rotunno 1989, 1990; Miranda and James 1992; Smith and Grønas 1993; Schär and Durran 1997). The splitting of streamlines, which accompanies the occurrence of a stagnation point, produces phenomena such as wave breaking, lee vortices, or upstream blocking. Different forcing mechanisms leading to vortex shedding were examined by Sun and Chern (1994), Peng et al. (1995), and Schär and Durran (1997). And recently the role of additional flow determining effects like vertical wind shear (e.g., Miranda and Valente 1997; Grubišić and Smolarkiewicz 1997; Shutts 1998), planetary rotation (e.g., Smith 1982; Thorsteinsson 1988; Trüb 1993; Thorsteinsson and Sigurdsson 1996; Bauer 1997), and surface friction (e.g., Grubišić et al. 1995; Olafsson and Bougeault 1997) were investigated.

Though one of the important parameters, comparatively few studies deal with the influence of the horizontal aspect ratio, that is, the ratio of spanwise to streamwise extension of an obstacle $\beta = L_y/L_x$, on mountain airflow. By means of perturbation theory, Scorer, as early as 1956, found that the vertical displacement of streamlines is stronger the larger the across-stream to along-stream barrier extension. More detailed analyses of stream patterns for linear flow im-

Corresponding author address: Dr. Manfred H. Bauer, Zentralanstalt für Meteorologie und Geodynamik, Regionalstelle für Tirol und Vorarlberg, Fürstenweg 180, 6020 Innsbruck, Austria.
E-mail: manfred.bauer@zamg.ac.at

pinging on different quasi-elliptic mountain shapes stem from Blumen and Dietze (1981) and Phillips (1984). Based on linear theory, Smith (1989a) constructed a regime diagram that reveals the occurrence of stagnation points as a function of H_m and β. He showed that for wide obstacles ($\beta > 1$) stagnation and ensuing wave breaking first start above the mountain leeside slope, whereas for long mountain ranges ($\beta < 1$) the fluid first stagnates near the surface on the windward side. Exemplary nonlinear numerical simulations were performed by Smolarkiewicz and Rotunno (1990) and Olafsson and Bougeault (1996). At $H_m = 3$ and β varying from 0.5 to 8, Smolarkiewicz and Rotunno found a qualitative consistency with predictions by Smith. Additionally, upstream propagating columnar modes occurred for wide mountains. The absence of this effect for long obstacles in spite of upstream stagnation indicates the existence of two distinct effects that can both lead to a deceleration of the flow. Leeward vortices form for $\beta < 1$ even though no windward stagnation can be observed, which is a hint of the independence of these two processes. Olafsson and Bougeault, on the other hand, simulated flow impinging on an obstacle with $\beta = 5$ for various H_m. For small H_m, results of linear theory were confirmed. For H_m higher than 3 no wave breaking occurred along the central axis through the mountain peak but still on both sides of the axis. They explained this phenomenon with the reduced pressure anomaly due to advection of denser air near the ground connected with reversed flow in the center of the two lee vortices. Flow modifications due to the consideration of the earth's rotation for various β were observed numerically by Thorsteinsson and Sigurdsson (1996) and Bauer (1997) for flow without wave breaking, and by Olafsson and Bougeault (1997) for large H_m and the special case of $\beta = 5$ and Rossby number $\mathrm{Ro} = U/fL = 2.25$ (where f is the vertical Coriolis parameter).

Castro and Snyder (1993) did not observed wave breaking in tank experiments in the lee of an axisymmetric Gaussian-shaped barrier before $H_m = 2.85$, whereas linear analysis gives a critical value of $H_m = 1.34$. On the one hand, factors like boundary reflections, friction, and nonhydrostatic effects become important in physical experiments. On the other hand, the stream patterns showed a strong dependence on the mountain shape, and also the steepness of the slope, so that their results are not interpretable as a function of H_m and β alone. In any case, for all mountain widths and lengths an upper limit of H_m (mostly between 5 and 10) was detectable above which the enormous stability suppressed any wave breaking.

The purpose of this work is a detailed and *systematic* examination of stream patterns as a function of the horizontal aspect ratio β, the ratio of across-stream to along-stream extension of the obstacle, by means of idealized numerical simulations (free-slip lower boundary, no rotation, uniform initial wind and stability). The final goal is a nonlinear counterpart to Smith's linear regime diagram for stagnation points.

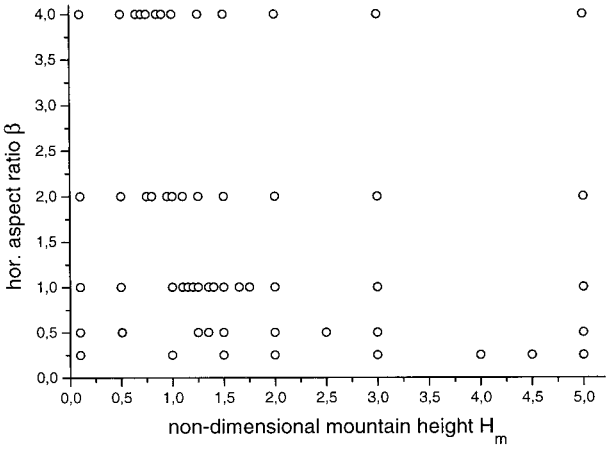

FIG. 1. ($H_m - \beta$) setting of the flow experiments in this study.

The paper is organized as follows. Section 2 gives a short description of the model setup and the design of the experiments. Section 3 covers the numerical results. For selected β, flow regimes are distinguished as a function of H_m. First, the prescribed flow impinges upon an axisymmetric barrier. In a second step, this barrier is stretched. Stream patterns for a wide mountain with $\beta = 4$ and a long mountain with $\beta = 0.25$ are examined. These values correspond approximately to the aspect ratio of the Alps for meridional and zonal flows, respectively. The range of H_m under consideration (see Fig. 1) is representative for realistic Alpine flow conditions. Taking a mountain height of $h_m = 3$ km, a buoyancy frequency N of 10^{-2} to 2×10^{-2} s^{-1}, and a typical wind speed U near the crest between 10 and 30 m s^{-1}, H_m varies between 1 and 3. Under certain conditions, of course, much lower or even higher H_m can be expected. At the end of section 3, more systematic simulations lead to a regime diagram for stagnation points and a representation of velocity extrema and drag as a function of H_m and β. Results are summarized in section 4.

2. Model setup

The following simulations were performed with the σ_z-model Regional Atmospheric Modeling System (RAMS), Version 3b, a limited-area primitive equation model developed at the Colorado State University. The model works with a terrain-following vertical coordinate,

$$\sigma_z = z_T(z - z_S)/(z_T - z_S), \tag{1}$$

where z_T indicates the model top, and $z_S(x, y)$ the height of the topography (Gal-Chen and Somerville 1975a,b). The atmospheric state is expressed by means of the momentum equation, an Exner-function tendency equation, and the thermodynamic energy budget. An ex-

TABLE 1. Used parameter values: β is the horizontal aspect ratio (width to length); $N(x)$ and $N(y)$ are the number of grid points streamwise and spanwise to the initial flow direction; t is the dimensional; T the nondimensional integration time.

$\beta = L_y/L_x$	$N(x)$	$N(y)$	t[hours]	$T = tU/L_x$
1	119	89	90	32.4
2	119	139	90	32.4
4	189	179	90	32.4
0.5	239	89	120	21.6
0.25	399	89	168	15.1

haustive review of this model and its abilities is given by Pielke et al. (1992). The applicability of RAMS within the framework of idealized three-dimensional simulations is demonstrated by Bauer (1997).

The airstream is assumed to be nonhydrostatic, compressible, nonrotational, and inviscid. Moist processes, radiation, and surface parametrizations are excluded. Initially the fluid moves with a speed of $U = 10$ m s^{-1} in a continuously stratified atmosphere with a constant Brunt–Väisälä frequency of $N = 0.01$ s^{-1}.

The grid was varied according to the obstacle size. The horizontal integration domain and integration time are listed in Table 1. The grid distance is $\Delta x = \Delta y = 20$ km. Here, 35 levels were used vertically. The layer thickness is 100 m at the ground and increases by a factor of 1.11 over the distance of a vertical length of a hydrostatic gravity wave ($\sim$6.3 km), remains constant with $\Delta z = 700$ m up to a height of about 11 km, and increases again with a factor of 1.11 up to about 21 km. The obstacle is introduced shocklike at the initial time. Its shape is Gaussian,

$$h(x, y) = h_m \exp\left[-\left(\frac{x - x_0}{L_x}\right)^2 - \left(\frac{y - y_0}{L_y}\right)^2\right], \quad (2)$$

where h_m is the maximum mountain height; x_0, y_0 are the coordinates of the mountain peak; and L_x, L_y the e-folding widths in the x and y directions. Compared to the gentler sloped bell-shaped mountain, it has the advantage of requiring a smaller grid domain. In case of a width to length asymmetry, the shorter mountain scale consists of at least $5\Delta x$ corresponding to 100 km. The time step is 60 s; for terms involving the propagation of sound waves it is 20 s.

A radiation condition is applied at all four lateral boundaries through a calculation after Klemp and Wilhelmson (1978). Upstream propagating disturbances can modify the inflow, since this scheme does not relax the flow toward initial conditions. Most of the results are presented at a time when an almost stationary state is reached but when the inflow is still almost unaltered. At the upper boundary, reflections of impinging energy are suppressed by means of a Rayleigh friction absorbing layer with a Rayleigh friction time of 3000 s. The strength of this ''sponge layer'' is zero at lower heights and increases linearly within the uppermost six levels (corresponding to a layer thickness of slightly more than one vertical wave length).

Aliasing is suppressed by a horizontal diffusion scheme according to Smagorinsky (1963). The turbulence parametrization used is a scheme of Mellor and Yamada (1982) modified by Helfand and Labraga (1988), which evaluates a budget equation for the tendency of turbulence kinetic energy. If the turbulence grow, a level 2.0 closure is used to calculate the diffusion coefficient. If it decreases, a level 2.5 closure is applied. The mathematical formalism can, for example, be found in Wolyn and McKee (1992).

The range of nondimensional mountain heights for a particular β where simulations were undertaken is indicated in Fig. 1. Additionally, simulations with $H_m = 7.5$ and 10 were performed for $\beta = 1$ and $\beta = 0.25$.

3. Simulation results

To enable a direct comparison to previous simulations by other authors, we first want to present flow regimes for an axisymmetric barrier. In the second part, regimes for a wide and a long barrier are juxtaposed. The aspect ratios $\beta = 4$ and $\beta = 0.25$ correspond approximately to a meridional or zonal flow impinging upon the Alps. Finally, diagrams for various flow characteristics as a function of H_m and β are presented.

a. Axisymmetric mountain ($\beta = 1$)

1) QUASI-LINEAR RANGE [$H_m = O(0.1)$]

The excitation of gravity waves leads to the formation of a stationary wave above the mountain with an upstream phase tilt. The velocity disturbances near the surface are almost *symmetric* with retardation on the windward side and speed up downstream of the mountain top. Results correspond well with linear theory (Smith 1980). For example, at $H_m = 0.1$ the numerically calculated drag differs from its linear counterpart by less than 0.5%.

2) WEAKLY NONLINEAR RANGE [$H_m = O(1.0)$]

At $H_m = 1.0$ (Fig. 2, panels a1, a2) isentropes slope strongly. The velocity perturbations have increased considerably, but the air still flows over the barrier along the central axis. Most obvious is the additional velocity minimum several e-folding widths downstream of the mountain top (Fig. 2, panel a2), which only occurs within the lowest decameters. This minimum, almost as strong as the windward one, is a purely nonlinear phenomenon and is therefore not detectable in Smith's (1980) analytical theory. The reason for this deceleration is that horizontal convergence downstream of the barrier increases with H_m due to a confluence of the flow deflected laterally around the obstacle and the portion that accelerates down the lee slope. Air that moves

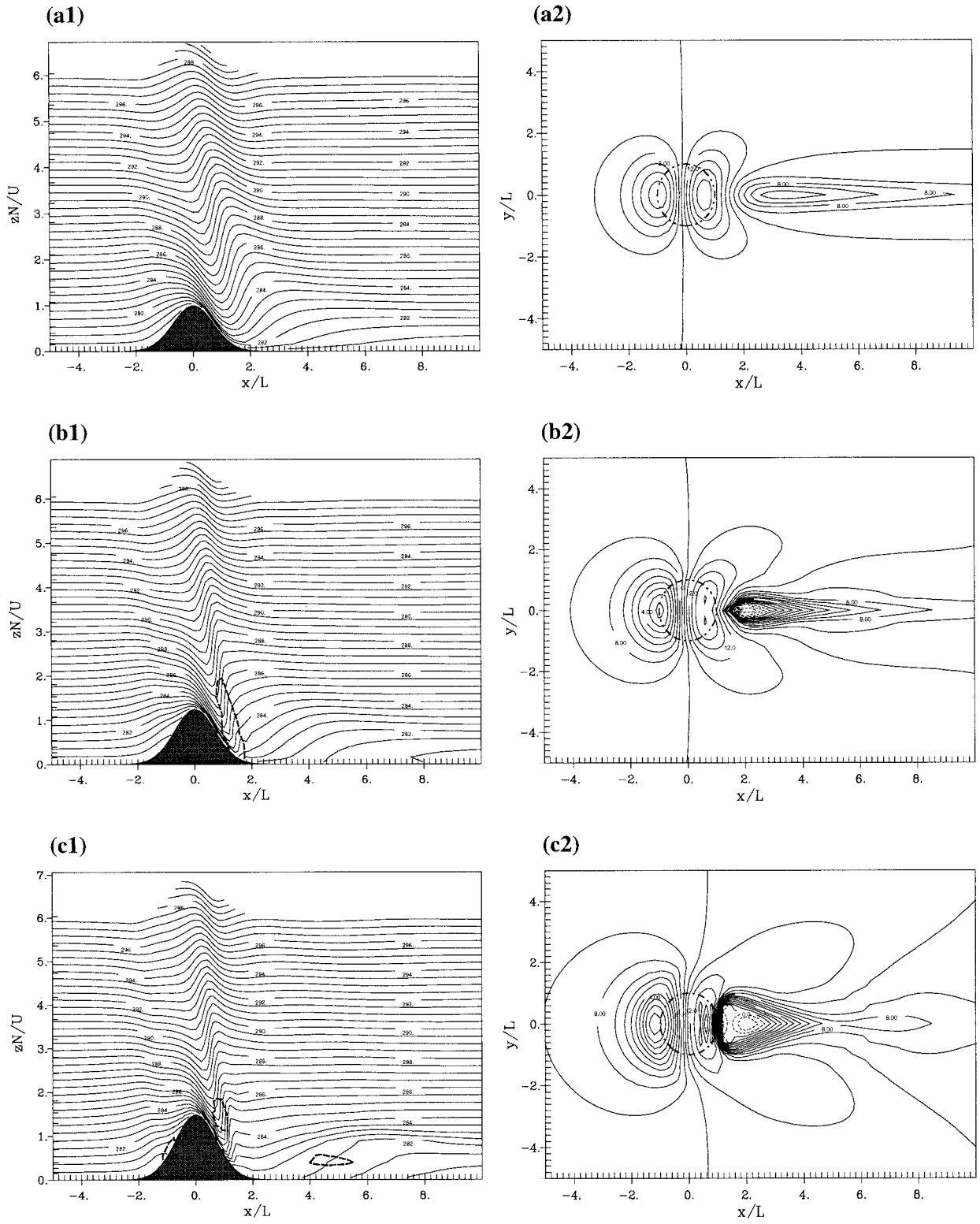

FIG. 2. (a1)–(c1) Vertical along-stream cross section of isentropes through the maximum mountain height with an interval of 0.5 K and the 0.1 $m^2 s^{-2}$ isoline of turbulence kinetic energy (dashed); (a2)–(c2) velocity component u in direction of the mean flow at ground level, with an interval of 1.0 m s^{-1} at (a) $H_m = 1.0$, (b) $H_m = 1.25$, and (c) $H_m = 1.50$. Separation point (saddle point) at the surface at S1 (S2) in (c1) and indicated with asterisk (filled circle) in (c2). Dash–dotted contour line indicates e-folding width L. Flow comes from the left side. Figures at nondimensional times (1) $T = 25.9$ and (2, 3) $T = 19.5$.

around the mountain flanks pushes underneath the potentially warmer air streaming down the lee slope and thereby lifts the isentropes off the ground (Fig. 2, a1).

3) WAVE BREAKING AND LEE VORTEX FORMATION WITHOUT WINDWARD STAGNATION ($1.15 \leq H_m < 1.40$)

Wave breaking, that is, the breakdown of the laminar flow due to the overturning of isentropes, first occurs at $H_m = 1.15$ and therefore at a lower H_m than predicted by linear theory (cf. Smith and Grønas 1993). The major criterion for the detection of wave breaking is a high value of turbulence kinetic energy (TKE). At the same nondimensional mountain height the air near the surface downstream of the mountain top stagnates. This leads to the generation of a counterrotating vortex pair with a *vertical* rotation axis about $2L$ downstream of the crest. The onset of wave breaking and the formation of lee vortices do not further reduce the windward velocity for any H_m. For $\beta = 1$ stagnation on the windward side is therefore *not* forced by lee-side effects, as Smith and Grønas (1993) argued. It does not occur until $H_m = 1.40$.

The stream pattern when wave breaking occurs but the air still flows *over* the obstacle along the central axis is shown in Fig. 2, panels b1, b2, for the case $H_m = 1.25$. The result is shown at a nondimensional time $T = tL_x/U = 19.5$ where the airflow has approximately attained a new quasi-stationary state different from the case without wave breaking; influences of upstream simulation area boundaries are not yet noticeable. Afterward only the lee vortices are still slightly weakening and moving downstream. This longer transient period of lee vortices is caused by dissipation, which acts over a longer timescale, as Schär and Durran (1997) stressed. The wave-breaking region is by far no perfect reflector; that is wave energy is not completely trapped below the zone of turbulent mixing. Significant vertical displacements at heights above the breaking zone (Fig. 2, b1) are detectable (cf. Olafsson and Bougeault 1996; Schär and Durran 1997).

Reverse flow does not occur on the windward side, where flow decelerates by 75%, but in the region of wave breaking and in the center of the two surface vortices about $2L$ downstream of the mountain peak (Fig. 2, b2). The evolution of the maximum wind speed is also remarkable. The velocity reaches its maximum *before* the stationary wave breaks. The simultaneous generation of reverse flow in the center of the leeside vortices prevents a stronger downward motion along the lee slope. A further increase of H_m decreases the strength of the surface wind maximum. The speed maxima move to the flanks $0.6L$ away from the central axis. This is fundamentally different from purely two-dimensional simulations where wave breaking drastically accelerates the flow.

The temporal transition into this quasi-stationary state is plotted in Fig. 3. At a time $T = 9.7$ (panels a1, a2) isentropes overturn vertically above the lee slope. The horizontal velocity is already slightly negative. Few time steps later the wave breaks and the production of turbulence kinetic energy begins. At that time the velocity $2.4L$ downstream of the mountain top is -0.7 m s^{-1} at the ground. Hence, air already moves back toward the obstacle *before* the wave breaks. The counterrotating vortex pair with vertical rotation axes forms close to the surface. Some nondimensional time steps later (panels b1, b2), a vortex with horizontal rotation axis occurs above the lee slope of the mountain. The turbulent zone propagates slightly leeward and downward, as can also be observed in simulations of a real foehn case (Georgelin 1997). The bold isoline, which marks the area where turbulence kinetic energy exceeds 10^{-1} m^2 s^{-2}, encloses the entire wake. The region with a velocity surplus decreases; the maximum along the central axis weakens from 16.0 to 15.0 m s^{-1}. The minimum near the surface on the lee side moves closer to the highest elevation and intensifies to -3.0 m s^{-1}. In the third row ($T = 16.2$) both originally independently generated recirculation areas have merged. At the time when the downward directed momentum transport reaches the surface, the reverse flow increases to -7 m s^{-1} for a short period before it weakens again and becomes constant at about -5.5 m s^{-1}. Even the vortex with horizontal rotation axis has attained a quasi-stationary state. The windward velocity is not influenced by the leeside wave-breaking event or by the formation of lee vortices. It first drops strongly, then only slightly, and remains almost unchanged at about 1.8 m s^{-1} for $T > 15$.

4) WAVE BREAKING, LEE VORTEX FORMATION, AND WINDWARD STAGNATION ($1.40 \leq H_m < 3$)

Linear theory overestimates the magnitude of the piling up of heavy air ahead of an obstacle. Whereas wave breaking starts earlier than would be expected by linear analysis, the windward standstill of the fluid is shifted to higher nondimensional mountain heights (Smith and Grønas 1993). RAMS reveals incipient negative velocities on the windward side at $H_m = 1.40$. For a further increase of H_m the zone of stagnant air spreads upstream. Moreover, there is an upper limit above which wave breaking happens just once during the entire simulation period, namely, within the first nondimensional time units due to the shocklike initialization. Afterward, the vertical transport of wave energy is too weak to produce another overturning of isentropes. Due to the numerical problems at very large nondimensional mountain heights this upper limit could not be exactly determined. At $H_m = 3.0$ the wind speed above the lee slope was slightly positive for nondimensional times $T > 10$, so that this upper limit should be near 3.0. Schär and Durran (1997) performed a simulation with $H_m = 3.0$ (but for a more gently sloping, bell-shaped mountain) showing a drastic reduction of the gravity wave signal. Their

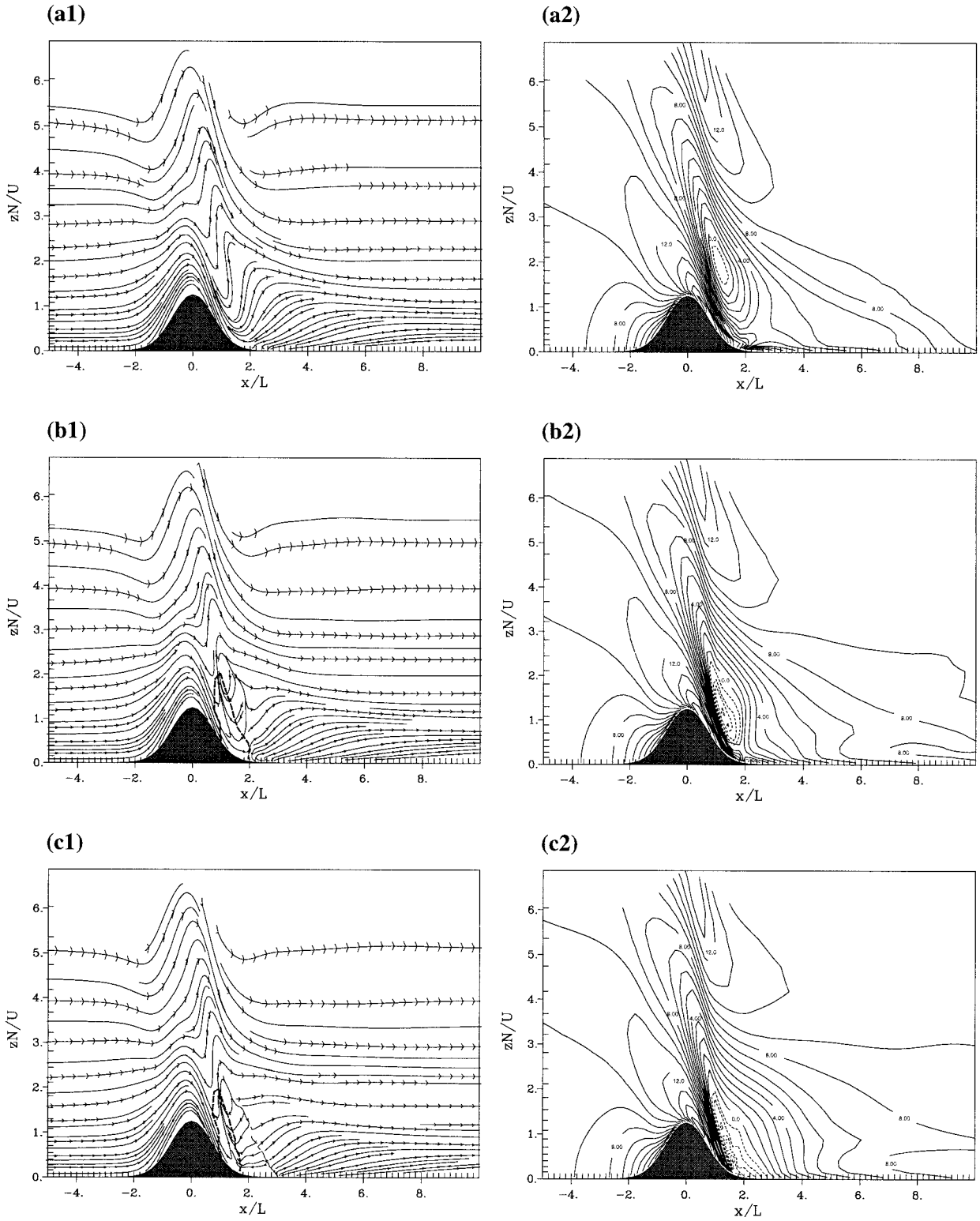

FIG. 3. Condition $H_m = 1.25$. Vertical along-stream cross section through the maximum mountain height: (a1)–(c1) Streamlines and the dashed 0.1 $m^2 s^{-2}$ isoline of turbulence kinetic energy; (a2)–(c2) velocity component u with an interval of 1.0 m s^{-1}; reversed flow indicated dashed. At nondimensional times (a) $T = 9.7$, (b) 13.0, and (c) 16.2. Flow comes from the left side.

results also show positive velocities above the lee slope, but they argue that weak wave breaking is present based upon the weak production of kinetic energy above the lee slope. Other authors, too, give a possible upper limit of wave breaking attained from laboratory experiments [e.g., Castro (1987): $H_m \sim 5$; Castro and Snyder (1993): $5 < H_m < 10$] or from simulations [Olafsson and Bougeault (1996) for $\beta = L_y/L_x = 5$: $H_m = 3.4$ along the central axis and $H_m = 6.8$ everywhere else]. From the examination of a (not commented) simulation result of Olafsson (1996, pp. 56–57) for a circular mountain at $H_m = 2.7$ one would infer that wave breaking does not occur there. Also the reverse flow in the center of the lee vortices strengthens with increasing H_m. The vortices spread spatially and start to shift downstream for about $H_m > 1.75$. For example, the center of the vortices at $H_m = 2.0$ is $2.5L$ downstream of the mountain top and one *e*-folding width wide.

The characteristic stream pattern for this scale range is presented for the case of $H_m = 1.50$. Figure 2, panel c1, shows the distribution of the isentropes. The θ surfaces do not descend as far on the lee side as for $H_m = 1.25$ (panel b1). At lower leeside levels, on the other hand, the strong reverse flow has become established. TKE is produced not only in the area of wave breaking but also about $5L$ downstream, where the air masses that flowed around the obstacle push underneath the almost stagnant air. This strong convergence leads to an unstable stratification as can be recognized from the large distance between isentropes in Fig. 2, c1. This process becomes stronger the larger H_m. Another area with unstable stratification and TKE production is situated one characteristic length upstream of the peak. Air has come to a standstill there and streams down the windward slope moving underneath colder air before it is deflected laterally (cf. Smolarkiewicz and Rotunno 1990; Olafsson and Bougeault 1996). The separation point where one part of the flow ascends the mountain while the other reverses moves slightly closer to the mountain top with increasing H_m. In contrast, the saddle point where the return flow meets the oncoming flow moves upstream. Overall, the reverse flow becomes more distinct and spreads over a larger region as H_m increases.

5) Windward stagnation and lee vortex formation without wave breaking ($3 \leq H_m$)

Numerical results were too perturbed in part of the simulation domain to examine this range in detail since spurious disturbances in the immediate lee of the obstacle occurred for large H_m (about $H_m \geq 2$). These high-frequency fluctuations were no amplification effects of $2\Delta x$ waves since a marked increase of the horizontal diffusion had no influence on their strength. The authors attribute these perturbations to well-known problems with the calculation of the horizontal pressure gradient and of the turbulence along steep slopes.

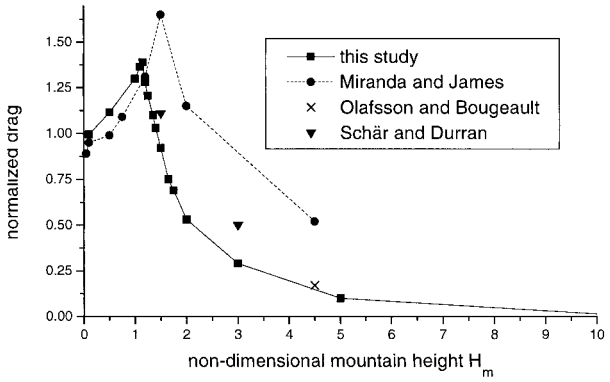

FIG. 4. Normalized three-dimensional drag as a function of the nondimensional mountain height H_m. Solid line with squares indicates results with RAMS (normalized with the drag of a linear hydrostatic flow across the same obstacle, $(2\pi)^{3/2}/16\rho_0 U_0 N_0 L h_m^2$). Dotted line with filled circles indicates results of Miranda and James (1992); the cross marks a result of Olafsson and Bougeault (1996); and the triangles represent simulations of Schär and Durran (1997). The last three results were calculated with the gentler sloped bell-shaped mountain and are normalized with $\pi/4\rho_0 U_0 N_0 L h_m^2$.

A simulation with $H_m = 10$ revealed high-frequency perturbations on the lee side of the barrier. Nevertheless, the tendency to increasing horizontal flow around the obstacle and vanishing vertical deflections in agreement with Drazin's (1961) potential flow was clearly visible. But still the vortex pair formed on the lee side, which is not included in Drazin's theory. The windward velocity distribution of RAMS simulations at high H_m was less disturbed. It showed a weakening of the reversed flow for $H_m > 3$, but a spreading upstream of the region of reduced velocity (cf. Smolarkiewicz and Rotunno 1990), which is consistent with Drazin's potential flow theory.

The last figure of this section (Fig. 4) summarizes the course of the three-dimensional normalized drag as a function of H_m. For the results with RAMS, values at the time $T = 19.5$ are plotted. First, the drag increases with H_m relative to the linear prediction. At $H_m = 1.15$, where wave breaking occurs at a later time, the normalized drag attains its maximum with 1.39. For $1.20 < H_m < 1.50$ the plotted value indicates the new quasi-stationary result after the onset of wave breaking. The simultaneous formation of lee vortices diminishes the pressure drop along the central axis and thereby reduces the drag. For $H_m > 1.45$, it is even smaller than in the linear case. For large H_m the drag oscillates within about $\pm 5\%$ of the plotted value due to the buildup and breakdown of wave overturning. The drag is computed up to $H_m = 10$ despite the numerical problems, since it is an integral quantity and small-scale oscillations have only a minor influence. For very large H_m the normalized drag asymptotically approaches zero since the flow is diverted around the barrier and moves quasi-two-dimensionally. No net force acts against the mountain. Numerical results are compared with simulations of three other researcher teams. Instead of the Gaussian-

shaped obstacle, they all used the more gently sloped bell-shaped mountain of the form

$$h(x, y) = h_m[1 + (x/L)^2 + (y/L)^2]^{-1.5}, \qquad (3)$$

which can lead to a delayed onset of wave breaking and windward stagnation, and to some differences of absolute values. The curve of Miranda and James (1992) seems to be an outlier. For $H_m = 1.5$ their normalized drag varies between 1.65 and 1.85 depending on the choice of h_m, N, and U. Another difference is that the drag increases *after* the onset of wave breaking. They also report such high-drag states in a more recent work (Miranda and Valente 1997). The other simulations in Fig. 4 and also simulations by V. Grubišić (1997, personal communication) contradict such a course in correspondence with the simulations of the authors.

b. Stretching of the barrier

1) Across-stream stretching

In this section the Gaussian-shaped barrier is stretched by a factor of 4 spanwise to the basic flow direction, that is, $\beta = L_y/L_x = 4$. The following flow regimes can be distinguished.

(i) Quasi-linear range [$H_m < O(0.1)$]

In contrast to the axisymmetric barrier, the perturbation distribution at $H_m = 0.1$ is already slightly asymmetric. The strongest positive deviation of u on the lee side is more distinct than the upstream deceleration effect. This is obviously an effect of nonlinearity which enhances lee-slope acceleration while reducing the tendency for windward stagnation (Smith and Grønas 1993). Also the pressure shows a stronger lee low than windward high. As a consequence, the drag already exceeds its linear counterpart by about 2% (for the derivation of the linear drag see the appendix).

(ii) Weakly nonlinear range ($H_m \sim 0.5$)

For wide mountains the wave amplitude, windward speed reduction, and leeward acceleration are much stronger than for $\beta = 1$ (Phillips 1984; Smith 1989a). Air is flowing predominantly over the obstacle. Lateral deflections are small and restricted to the mountain edges (cf. Bauer 1997).

(iii) Wave breaking without windward stagnation or lee vortex formation ($0.70 \leq H_m < 0.90$)

Wave overturning begins at $H_m = 0.70$ [cf. $H_m = 0.75$ for an infinitely wide Gaussian-shaped mountain barrier according to Pierrehumbert and Wyman (1985)]. Figure 5 shows the temporal evolution of the flow by means of isentropes and surface wind speed at a slightly higher H_m ($H_m = 0.75$). With the onset of wave breaking leading to the production of turbulence kinetic energy at $T \sim 11.9$ (Fig. 5, a1, a2), energy is reflected back to the ground; the turbulent wake spreads downward. Isentropes are strongly compressed. The speed maximum occurs underneath the wake at $T = 15.1$ (panels b1, b2) with more than 22 m s^{-1}. The turbulent wake extends from the region of wave breaking downstream and to lower heights but does not reach the ground. Instead, the isentropes close to the surface spread again slightly so that the maximum wind speed is reduced again. The strong low-level flow expands farther down the lee slope and leads to an increasing downstream shift of the turbulence zone at lower heights, even after $T = 30.2$ (Fig. 5, c1, c2). The maximum of the u component at the surface changes its location with time. The wave breaks not only above the central axis but also within a zone that spreads about $y = 0$ with a width of $\pm L_y/2$. Since isentropes do not overturn everywhere simultaneously, the wind maximum shifts from the center to both sides (about $1.4L_x$ away from h_m) and back again with time. The air $4L_x$ downstream of h_m is far from stagnation for all T since the confluence of air masses that have been diverted laterally by the barrier is weak. Hence, for $\beta > 1$ wave breaking occurs *before* lee vortices form.

In Fig. 6 wind extrema and drag are plotted as a function of time. The curve $u_{\max}$ peaks when the reflected energy coming from the onset of wave breaking reaches the ground and remains almost constant at about twice the basic flow speed thereafter. Therefore, the maximum wind speed increases considerably *after* the onset of wave breaking. Upstream and downstream velocity minima show a very weak tendency of intensification. A real stationary state has not been reached by the end of the simulation, yet. The drag, as a consequence, keeps on growing to a classical high-drag state with almost twice the linear drag.

(iv) Wave breaking, lee vortex formation, and windward stagnation ($0.90 \leq H_m < ?$)

When $H_m = 0.90$ is exceeded, lee vortices on the lee side of the barrier form close to the surface. Moreover, windward stagnation also first occurs at about $H_m = 0.90$. Compared to previous studies this is a rather low value: Pierrehumbert and Wyman (1985) observed blocking in their two-dimensional simulations not before $H_m = 1.5$; Olafsson and Bougeault (1996) determined complete stagnation for $H_m = 1.4$, but they performed no simulations in the range $1.0 < H_m < 1.4$ and used the less steep bell-shaped mountain.

The time evolution of the velocity distribution at nondimensional mountain heights slightly above this critical value is plotted in Fig. 7 for $H_m = 1.0$ as an example. The stronger vertical energy flux leads to an earlier overturning of isentropes (at $T \sim 7$). The ensuing turbulence zone expands downward and downstream. In contrast to the before-mentioned case $H_m = 0.75$, the momentum transport is strong enough to penetrate to the surface.

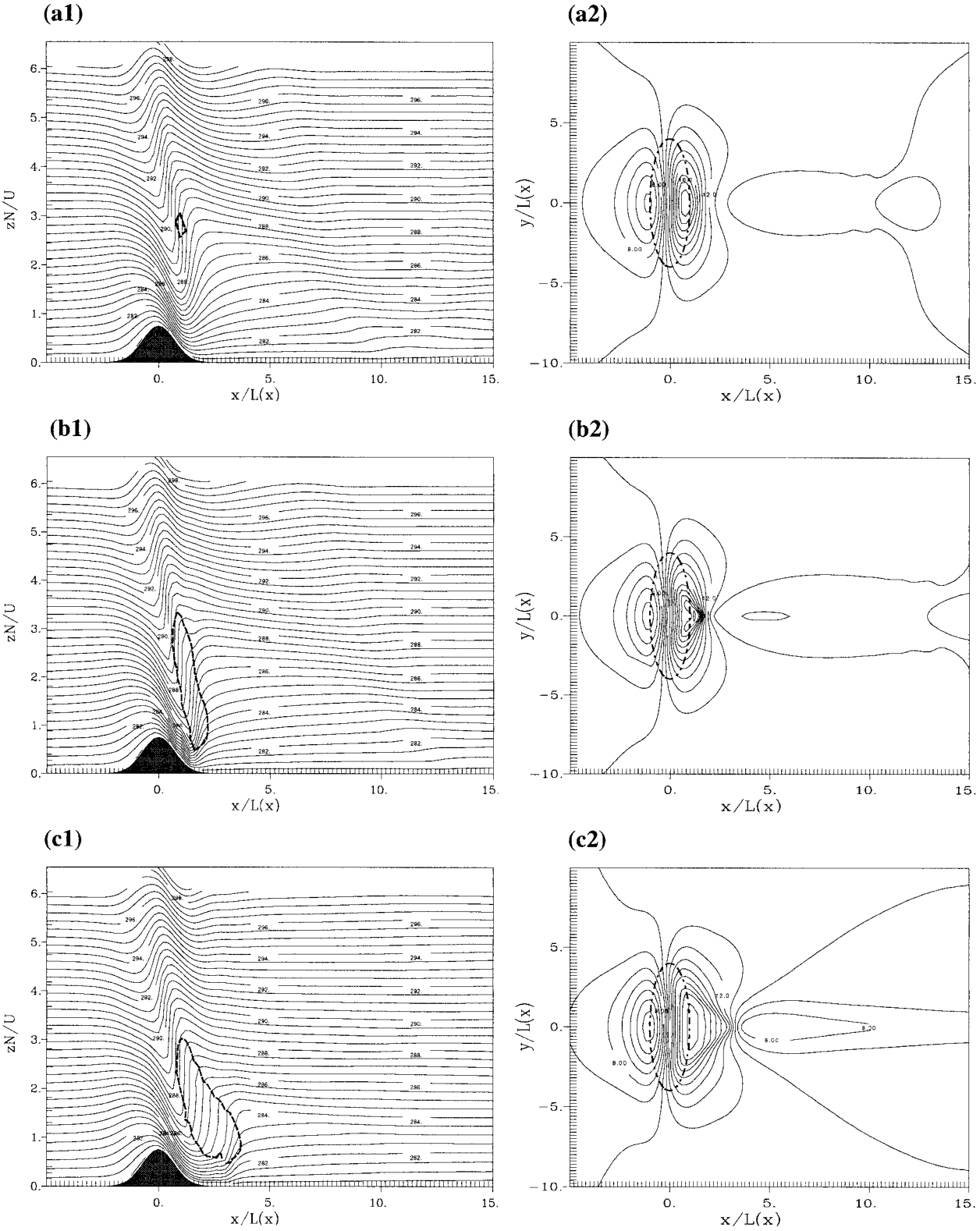

FIG. 5. Condition $H_m = 0.75$, $\beta = 4$. (a1)–(c1) Vertical along-stream cross section of isentropes through the maximum mountain height with an interval of 0.5 K and the dashed 0.1 $m^2\ s^{-2}$ isoline of turbulence kinetic energy; (a2)–(c2) surface velocity component u with an interval of 1.0 m s^{-1}; reversed flow indicated dashed. At nondimensional times (a) $T = 11.9$, (b) 15.1, and (c) 30.2. Flow comes from the left side. Contour line indicates e-folding width L.

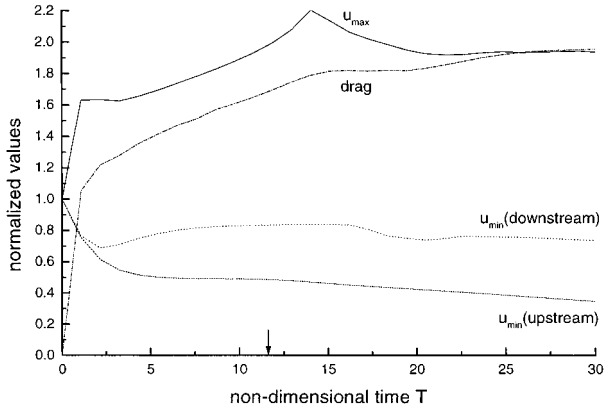

FIG. 6. Condition $H_m = 0.75$, $\beta = 4$. Temporal evolution of relative velocity disturbances and of the normalized drag. Here, T indicates the nondimensional time tL/U. Velocities are normalized with the basic flow ($U = 10$ m s^{-1}): Velocity maximum at the surface, solid; velocity minimum on the windward side, dashed; velocity minimum on the lee side, dotted. Drag normalized with the drag of a linear hydrostatic flow across the same obstacle, derived in the appendix (dash–dotted). The arrow marks the onset of wave breaking.

The low-level jet, which extends several mountain lengths down the lee slope (panels a1, a2), is pushed back to the immediate lee (panels b1, b2). Whereas the leeward deceleration is only weak and far from stagnation shortly after the wave breaks ($T = 7.6$, panel a2), the wind speed drops rapidly below zero at $T = 14.0$ (panel b2). At this time, lee vortex formation at the surface is *triggered* by the wave-breaking process. This suggests that, in contrast to the axisymmetrical case of section 3.a, wave breaking and lee vortex formation are *not* independent results of increased nonlinearity for $\beta > 1$. The vortex pair would *not* form for such a small H_m, if the wave above the lee slope would not break. With time the reversed flow in the center of the vortices strengthens considerably, moves downstream, and decouples from the turbulence zone produced by wave breaking (panels c1, c2).

Figure 8 shows a vertical isentropic cross section and the streamlines at ground level at $T = 30.2$. The horizontal mass confluence at the saddle point $5L_x$ downstream of the peak lifts the isentropes from the ground (panels a1, a2). This unstably stratified region is also the downstream limit for the zone of TKE. The form of the vortex pair at the surface changes with time. After the sudden onset of lee vortex formation at $T = 14.0$ the vortices first become wider; then they elongate considerably. Olafsson and Bougeault (1996) ended their simulations at a rather early stage of vortex formation ($T = 16.2$); Smolarkiewicz and Rotunno (1990) even stopped at $T \sim 9$. Therefore their vortices (see Olafsson and Bougeault's Fig. 2, pp. 2468f; Smolarkiewicz and Rotunno's Fig. 11, p. 1507) are still very ''egg-shaped.'' The present simulation reveals that even at $T = 30.2$ the vortices still change slightly, although the strongest reverse flow is almost constant and stationary slightly less than $2L_y$ downstream of h_m (Fig. 8b).

What about the windward velocity distribution? Stagnation begins $1.2L_x$ upstream of the mountain peak at $T \sim 10$. In contrast to the axisymmetric case, the blocking zone does not become stationary at an early stage of the simulation but extends upstream and strengthens with time (Fig. 7). Columnar modes propagate against the basic flow extending the zone of reduced flow speed progressively farther upstream as time passes. For example, the contour line of $u = 9$ m s^{-1} at the surface propagates with a nondimensional speed $c = -0.18$, $u = 8$ m s^{-1} with $c = -0.08$ and $u = 4$ m s^{-1} with $c = -0.03$. This jump in the upstream condition is connected to the onset of wave breaking, whereby horizontally propagating waves are excited (Pierrehumbert and Wyman 1985; Smolarkiewicz and Rotunno 1990; Garner 1995). Interpreting their simulation results, Smolarkiewicz and Rotunno (1990) already stated that upstream propagating columnar modes are absent for $\beta = 1$ but that they appear with increasing strength as the mountain becomes wider due to a more vigorous wave breaking. This is confirmed by the present simulations. Therefore, for $\beta > 1$ two processes coexist that can decelerate the flow ahead of the obstacle and lead to complete stagnation: the piling up of heavy air [called the ''background disturbance'' or ''initial surge'' by Garner (1995)] and the excitation of upstream propagating waves (called the ''wave-breaking surge''). Still, the predominant deceleration effect stems from the blocking of the impinging fluid, although the flow would probably not come to stagnation for $H_m = 1.0$ without columnar modes. According to Garner (1995) these modes produce no permanent upstream alteration, in contrast to Pierrehumbert and Wyman's (1985) assumption, but they are temporary transients with a very long timescale of $T = 25$ to $T = 35$. A weakening of the upstream speed reduction could not be detected in the present computational results since the integration time was too short.

The superposition of the before-mentioned two deceleration effects leads to the slow drop of the windward minimum below zero in Fig. 9. On the other hand, the minimum at the leeward foothills first decreases only by 20%. When the turbulence zone due to wave breaking reaches the surface, speed is rapidly reduced by more than 10 m s^{-1}. The maximum wind speed remains slightly below twice the strength of the basic flow. At the beginning of the simulation, the drag increases to almost 2.8 times its linear value, but then drops to about 2.0 and shows a weak tendency to increase with time afterward. The leeside vortices are too small to influence the drag significantly.

Figure 10 presents results at $H_m = 1.5$ for $T = 19.5$ and $T = 30.2$, a time when most previous related three-dimensional simulations have already stopped (cf. Smolarkiewicz and Rotunno 1989, 1990; Olafsson and Bougeault 1996). A considerable evolution within this time

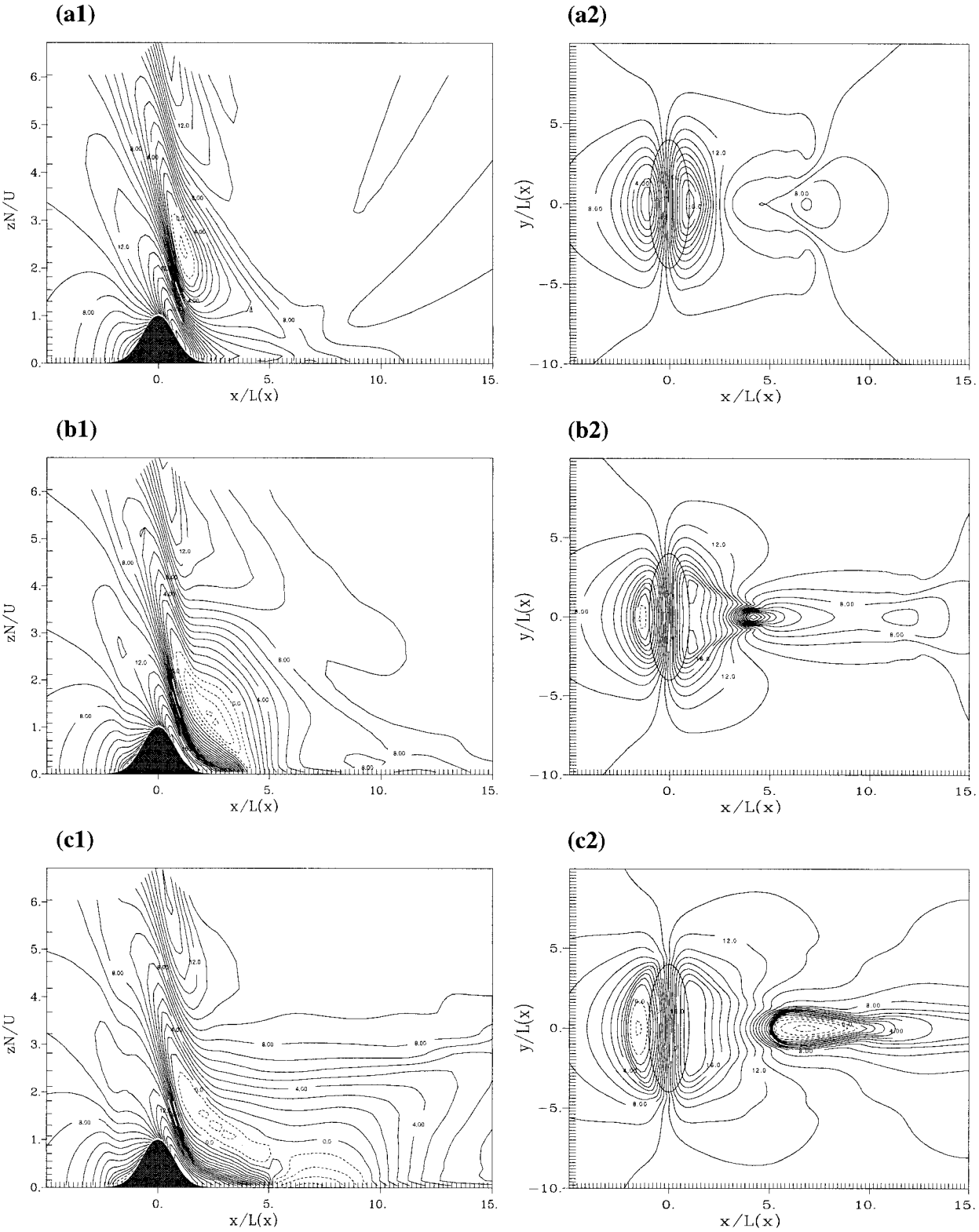

FIG. 7. Condition $H_m = 1.0$, $\beta = 4$. (a1)–(c1) Vertical along-stream cross section in direction of the mean flow through the maximum mountain height and (a2)–(c2) surface value of the velocity component u with an interval of 1.0 m s^{-1}; reversed flow indicated dashed. At nondimensional times (a) $T = 7.6$, (b) 14.0, and (c) 30.2. Flow comes from the left side. Contour line indicates e-folding width L.

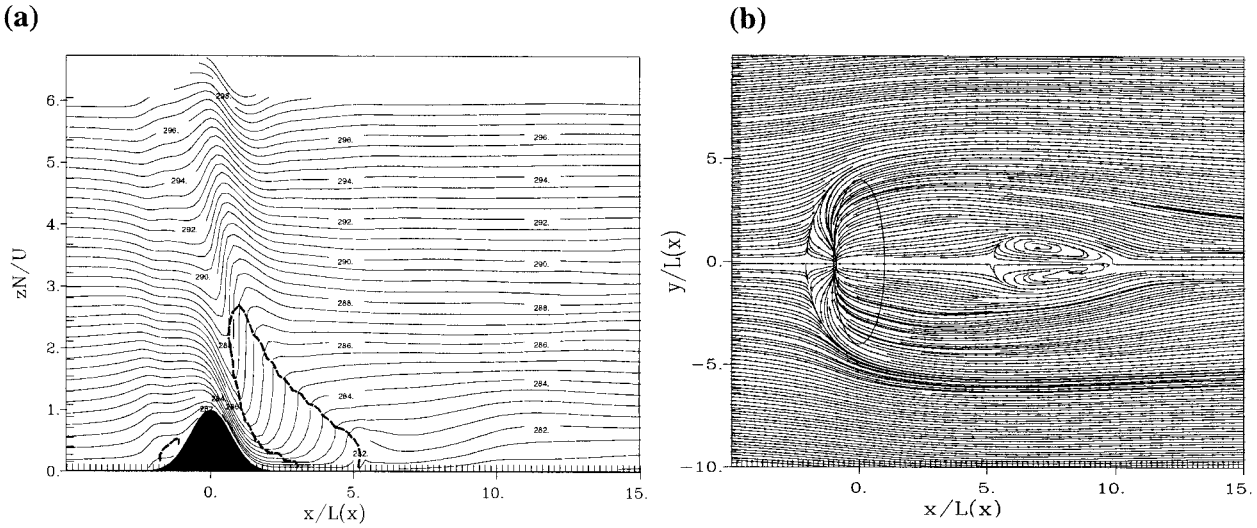

FIG. 8. Condition $H_m = 1.0$, $\beta = 4$. (a) Vertical along-stream cross section of isentropes through the maximum mountain height with an interval of 0.5 K and the dashed 0.1 m^2 s^{-2} isoline of turbulence kinetic energy and (b) streamlines at ground level at a nondimensional time $T = 30.2$. Contour line indicates *e*-folding width *L*. Flow comes from the left side.

interval can be detected (and the stream pattern is still not stationary at the end of the presented simulation). The reverse flow in connection with the lee vortices has slightly intensified and expanded both downstream and toward the barrier (Fig. 10b). The latter weakens the maximum wind speed along the central axis, since the fluid acceleration down the lee slope is restricted to near the mountain top. The maximum wind speed moves more and more to the lateral mountain edges, where air accelerates over and around the ridge. Furthermore, strong winds can be found 5 to 10*L* downstream of the peak, sideways of the central axis, building a strong shear zone with the interior vortices. The vortex pair elongates and widens to cover the entire mountain *e*-folding width (Fig. 10c). Compared to $H_m = 1.0$ the reverse flow has intensified, the vortices have grown, and their centers have moved away from the central axis, but the distance to the mountain peak remains about the same (between 7 and $8L_x$; cf. Olafsson and Bougeault 1996). Furthermore, a strong cold-air dome in front of the barrier (Fig. 10a) exists during the entire simulation period. The blocked air overturns vertically, flows backward down the windward slope, and deflects laterally. Thereby, secondary gravity waves are excited. The upstream influence is more intense than at $H_m = 1.0$. This is caused by a stronger background disturbance due to a marked blocking of heavy air in front of the barrier and also caused by stronger columnar modes. They entail about a doubling of the propagation speed of the velocity-deficiency contour lines.

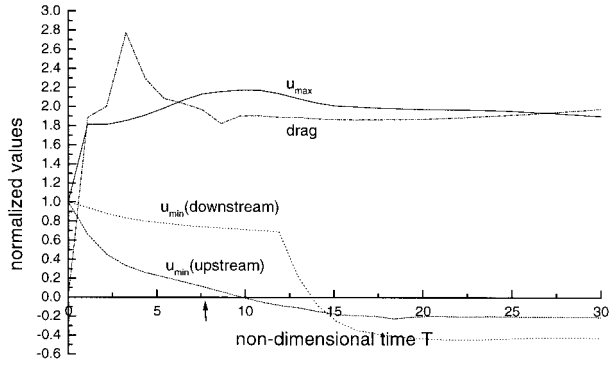

FIG. 9. As in Fig. 6 but for $H_m = 1.0$ and $\beta = 4$.

The temporal evolution of the velocity extrema is plotted in Fig. 11. The reverse flow on either side of the barrier is more intense than at $H_m = 1.0$. But the most obvious difference is the weakening of the maximum wind speed with time. The growth of the vortices expands the zone of reversed flow closer to the mountain top. Thereby, the descent of potentially warmer air along the lee slope and the wave formation are hindered (cf. Olafsson and Bougeault 1996). The wind maximum shifts more and more to the lateral mountain edges and becomes continuously weaker. This dampening of the downslope wind produces a clear drop of the drag from a high-drag state to nearly linear values.

(v) Lee vortex formation and windward stagnation without wave breaking

Computational difficulties, mentioned at the beginning of this chapter, prevent an evaluation of the upper limit of wave breaking. Therefore, only a reference to results of Olafsson and Bougeault (1996) is made. For a bell-shaped mountain with $\beta = 5$ they determined that wave breaking ceases along the central axis at $H_m = 3.4$ (due to the dampening of wave formation by the strong leeward vortices) but that isentropes overturn on

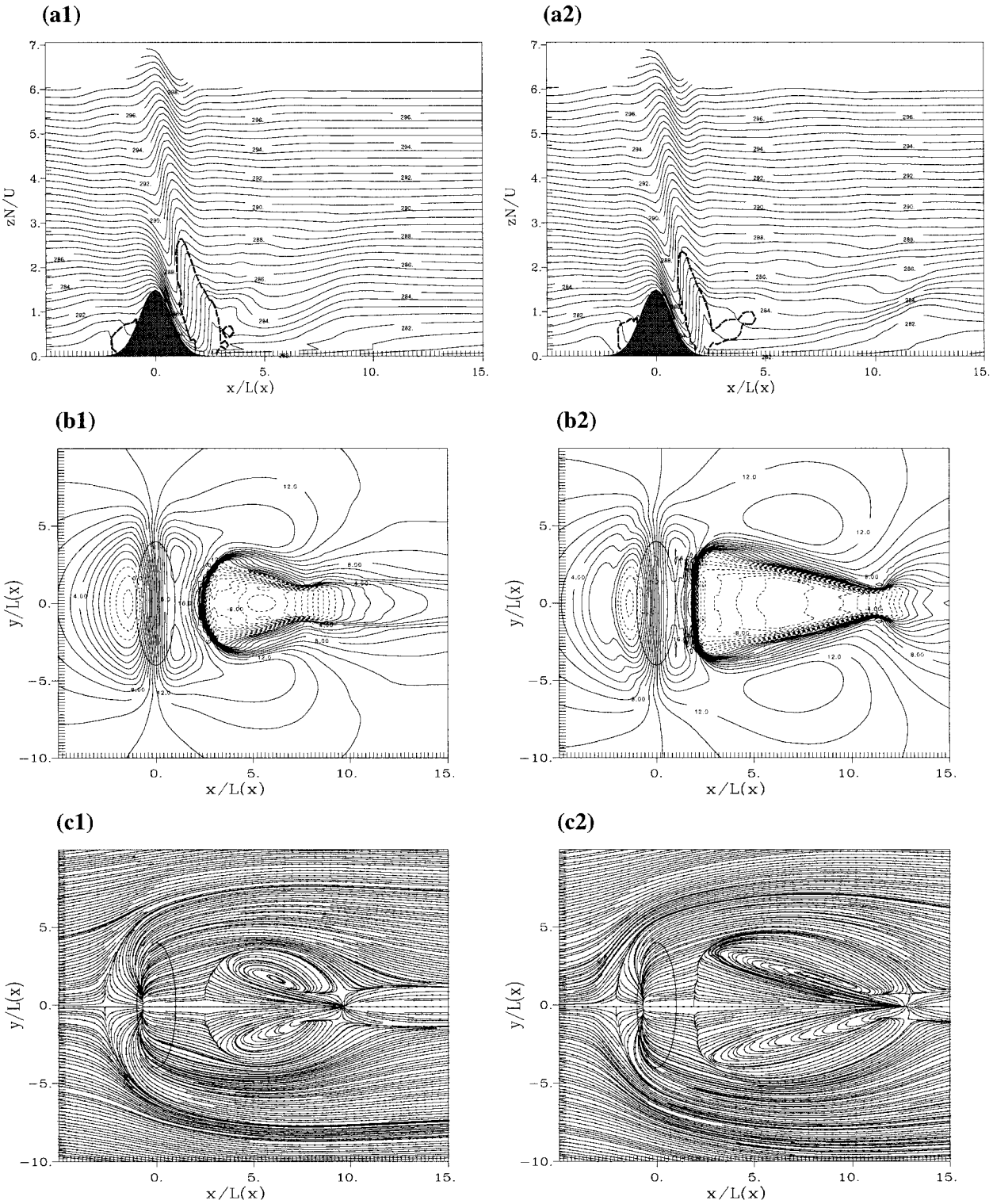

FIG. 10. Condition $H_m = 1.5$, $\beta = 4$. (a) Vertical along-stream cross section of isentropes through the maximum mountain height with an interval of 0.5 K and the dashed 0.1 $m^2\ s^{-2}$ isoline of turbulence kinetic energy, (b) velocity component u at ground level with an interval of 1.0 $m\ s^{-1}$, and (c) surface streamlines. Reversed flow indicated dashed. Contour line indicates e-folding width L. Flow comes from the left side. Figures at nondimensional times (1) $T = 19.5$ and (2) 30.2.

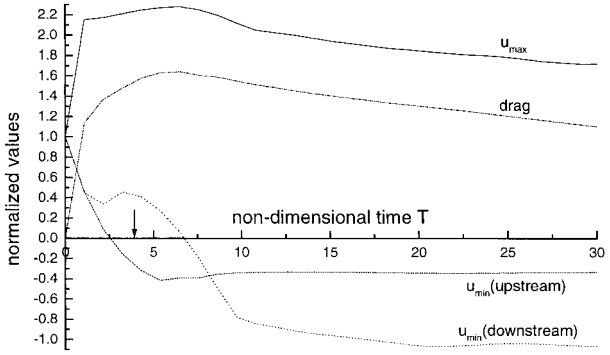

FIG. 11. As in Fig. 6 but for $H_m = 1.5$ and $\beta = 4$.

each side of it up to $H_m = 6.8$. For such a high mountain, lee vortices still form and windward stagnation occurs as well. Similar critical values can be expected for the steeper Gaussian-shaped mountain used in this study with $\beta = 4$. A control run with $H_m = 10$ was performed, which, indeed, revealed windward blocking and prominent vortices despite the numerical deficiencies on the immediate lee side.

2) ALONG-STREAM STRETCHING

In this section the Gaussian-shaped mountain is stretched by a factor of 4 in the direction of the basic flow, that is, $\beta = 0.25$. Flow patterns can be distinguished as follows.

(i) Sublinear range without wave breaking, lee vortex formation, or windward stagnation ($H_m < 4.5$)

At $H_m = 0.1$ the perturbations of the mean flow are very small; in correspondence with linear theory (Smith 1989a) wind maxima and minima are clearly less pronounced than for $\beta = 1$.

At $H_m = 1.5$, a height where isentropes overturn above the lee slope for mountains with $\beta \geq 1$, the vertical isentropic displacement is still very small for $\beta = 0.25$ (Fig. 12, a1). The same is true for the streamwise velocity perturbation (Fig. 12, a2). Most of the air is diverted laterally by the obstacle. Therefore, potentially warmer air reaches the ground. The strong convergence of cold air on the lee side of the barrier decelerates the flow along the central axis to less than 6 m s^{-1}. But the air is still far from stagnation up- or downstream of the obstacle. At $H_m = 3.0$, for example (not shown), the deceleration zone in front of the barrier expands far upstream. The air does not stagnate but the fluid is already slowed down by 20% two mountain lengths upstream of the crest, and by ⅔ one L_x upstream. Along the lee slope the air is pushed back towards the center. This effect entails a velocity reduction of about 70%. The maximum wind speed along the central axis has moved close to the mountain top. But for $H_m \geq 2$ the overall maximum is located about $2L_y$ sideways. The confluence of air deflected by the long barrier leads to a distinct acceleration along the upstream side of the mountain flanks. The wind maximum at $H_m = 2$ lies about $3L_y$ downstream of the axis through the mountain peak and shifts upstream close to ($x = 0$, $y = 2L_y$) with increasing H_m. The velocity distribution is stationary; *no* upstream propagating columnar modes occur.

(ii) Lee vortex formation without wave breaking or windward stagnation ($4.5 < H_m < 7.5$)

For long mountains, lee vortices form *without* wave breaking (cf. Smolarkiewicz and Rotunno 1990). But very high mountains are necessary to produce vortices on the lee side of a long mountain. Simulations with $H_m > 4.5$ revealed leeside wind speeds dropping below zero.

Figure 12, panel b1, b2 shows a simulation with $\beta = 0.5$ and $H_m = 1.5$. This example demonstrates a case of lee vortex formation with neither wave breaking nor wave overturning on the windward slope. The velocity field shows a minimum wind speed above the mountain top of more than 3 m s^{-1}; that is, the wave is far from overturning. Additionally, the flow upstream of the mountain peak is everywhere stronger than 3 m s^{-1} and still far from stagnation. Lee vortices form since the deceleration of air along the lee slope has become strong enough for stagnation and even flow reversal to occur. The violation of potential vorticity (PV) conservation forces the formation of lee eddies (Smith 1989b; Schär and Durran 1997). The dissipative process leading to PV generation is the overturning of isentropes at the stagnation point close to the surface downstream of the barrier. The vortex pair is not triggered by stagnation somewhere else in the flow field but by local wave breaking. The vortices are slightly downstream of the mountain *e*-folding width, which is similar to the experiment with $\beta = 1$ but differs from $\beta = 4$ where the vortices are clearly farther downstream (cf. Fig. 8). TKE is generated at the upstream end of the vortices where the reverse flow hits the flow streaming down the lee slope leading to a strong upward and lateral motion.

(iii) Lee vortex formation and windward stagnation without wave breaking ($H_m > 7.5$)

The oncoming air stagnates in front of the barrier for about $H_m > 7.5$. The fluid is diverted around the obstacle almost two-dimensionally. Therefore, wave breaking does not occur at *any* mountain height for such a long mountain range.

c. Stagnation points, velocity, and drag as a function of β

In this section the first appearance of stagnation points, the velocity distribution, and the drag are com-

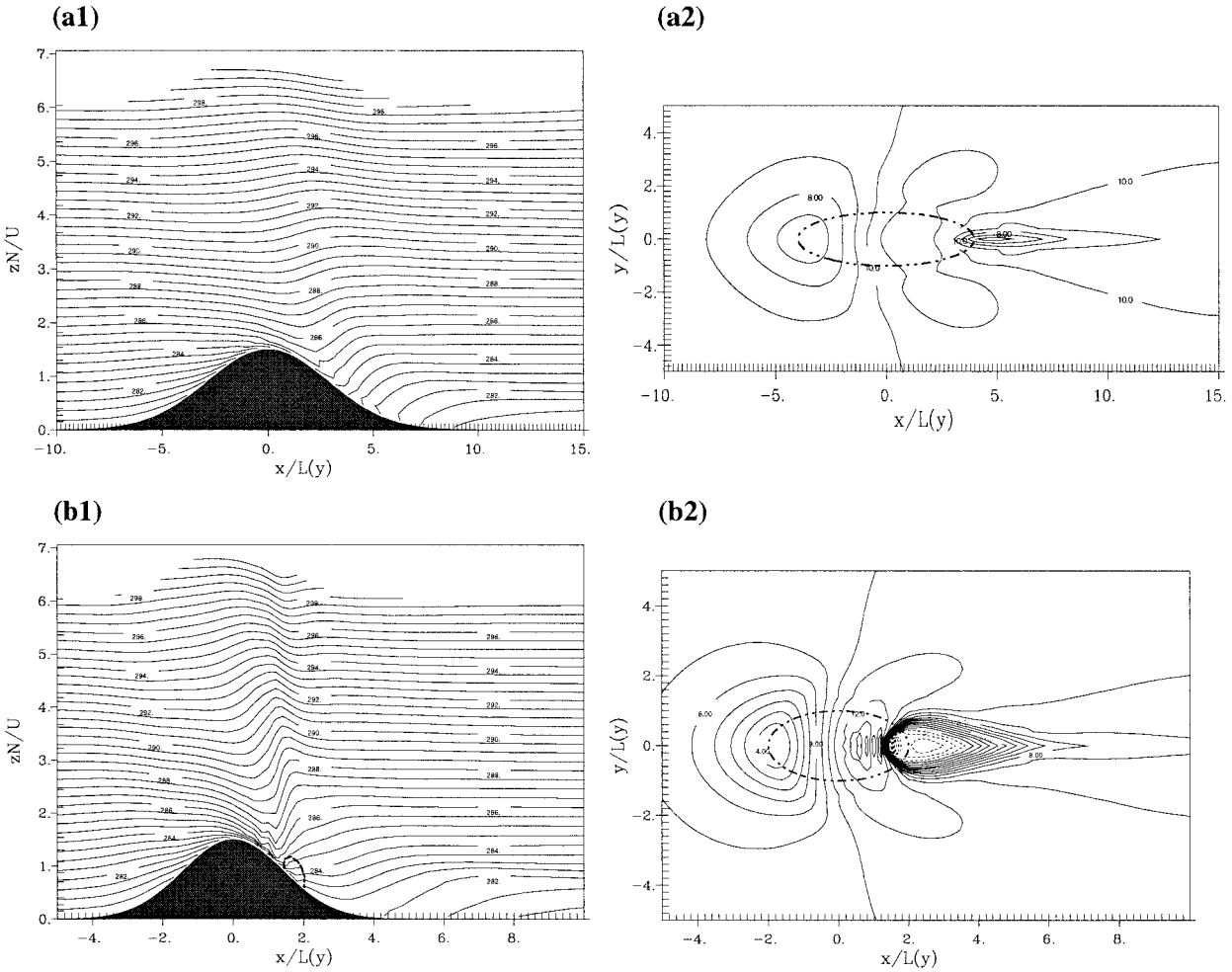

FIG. 12. Condition $H_m = 1.5$, (a) $\beta = 0.25$ and (b) $\beta = 0.5$. (1) Vertical along-stream cross section of isentropes through the maximum mountain height with an interval of 0.5 K and the dashed 0.1 $m^2 s^{-2}$ isoline of turbulence kinetic energy; (2) velocity component u at ground level with an interval of 1.0 m s^{-1}, reverse flow indicated dashed. Contour line indicates e-folding width L. Flow comes from the left side. Figures at nondimensional times (1) $T = 15.1$ and (2) 21.6.

pared for the axisymmetric mountain and the elongated mountains stretched by a factor 2 or 4 streamwise or spanwise to the basic flow. The values plotted are not always in a steady state (especially for wide mountains), but represent the momentary state at the end of the simulation (see Table 1).

Figure 13 shows the critical curves for the onset of stagnation points. The upper figure is reprinted from Smith (1989a) and represents results from linear theory. For the axisymmetric barrier leeside wave breaking and windward stagnation begin at the same threshold ($H_m = 1.34$). For long obstacles ($\beta < 1$) the flow upstream stagnates before the wave above the lee slope breaks; for wide obstacles ($\beta > 1$) the opposite is the case. Smith already mentioned the possible invalidation of the curves when one of the stagnation points has already occurred; therefore, his lines are partially dotted.

The strongly nonlinear results of the present simulations are plotted in the bottom figure. For $\beta = 1$, wave breaking appears *before* the air upstream of the barrier is completely blocked (cf. Smith and Grønas 1993). Nonlinearity decreases the threshold of wave breaking to $H_m = 1.15$. The larger β the smaller this critical H_m. Furthermore, an upper limit for wave breaking exists. An exact evaluation of this additional critical curve was not possible due to the previously mentioned numerical difficulties. The curves for the onset and for the end of wave breaking have to cross in between $\beta = 1$ and $\beta = 0.5$, since for $\beta \leq 0.5$ no wave breaking occurs for any H_m.

Stagnation upstream of the mountain is dampened by nonlinearity (Smith and Grønas 1993). For the axisymmetric barrier it first occurs at $H_m = 1.40$. The larger β the smaller mountains are necessary to produce windward stagnation. For wide mountains the onset of blocking is close to the linear prediction (despite its physical

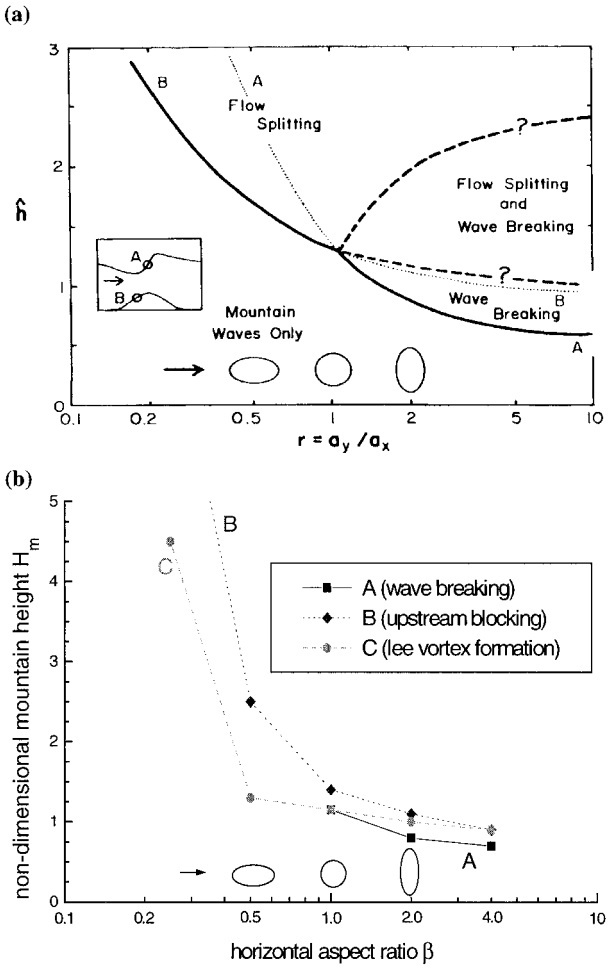

FIG. 13. Flow regimes as a function of the nondimensional mountain height H_m and of the horizontal aspect ratio $\beta = L_y/L_x$ [r in (a)]. Curve A indicates the onset of wave breaking; curve B marks the first appearance of stagnation on the windward side; and curve C shows the onset of lee vortex formation (corresponding to stagnation on the leeward slope). (a) Smith's (1989a) linear regime diagram. Curves are dotted where linear theory is not valid due to the occurrence of a stagnation point. Dashed lines indicate Smith's assumptions of possible other regime boundaries. (b) Numerical results of this study. Solid, wave breaking; dotted, upstream blocking; dashed, lee vortex formation.

invalidity). For long barriers the strong lateral deflection strongly dampens the windward deceleration. Very high mountains are necessary to produce upstream reverse flow.

In addition to Smith's linear analysis, a third stagnation point occurs in the flow field. Downstream of the mountain crest, flow can reverse close to the surface; a counterrotating vortex pair with a vertical rotation axis forms. Wave breaking is not necessary to induce these vortices, since they also exist for $\beta \leq 0.5$, where no wave breaking can be detected. However, for $\beta > 1$ leeward stagnation at the surface is triggered by wave breaking; the convergence of air, which was deflected laterally upstream of the barrier, would not be strong enough to produce such a strong deceleration. As a consequence, lee vortices begin to appear already for lower H_m when β is increased.

Figure 14 shows the different surface velocity extrema as a function of H_m and β at a time when the integrations have been terminated. In the weakly nonlinear range the maximum wind speed is larger the larger β. For the axisymmetric case $u_{\max}$ occurs before the wave breaks and lee vortices form. The latter dampens the leeward extension of downslope flow due to the increasing strength of reverse flow. For wide barriers the maximum wind speed increases with the onset of wave breaking and produces a so-called downslope windstorm. But with the formation and growth of the lee vortices for even higher H_m the acceleration zone and its magnitude are reduced again. The strength of the windstorm and the range of H_m where it occurs is larger for larger β. For long mountain ranges the wind maximum shifts from the central axis about $2L_y$ to both sides for large H_m (e.g., for $H_m \geq 3$ at $\beta = 0.5$ and for $H_m \geq 2$ at $\beta = 0.25$) and moves more and more upstream (e.g., $\beta = 0.25$: $u_{\max}$ at $x = 2.2L_y$ for $H_m = 2.0$, at $x = 0.6L_y$ for $H_m = 3.0$, and at $x = -1.6L_y$ for $H_m = 5.0$). The maximum increases continuously and exceeds the values for $\beta > 1$ for very high mountains.

The windward deceleration (Fig. 14b) in the weakly nonlinear range is stronger for larger β. For long mountains the speed reduction grows continuously within the plotted range of H_m but has still not come to a halt at $H_m = 2.0$. The minimum wind speed is close to $(-L_x, 0)$ and moves only slightly upstream with increasing mountain height. For $\beta = 1$ the wind reverses along the upstream slope for $H_m \geq 1.40$. For a further increase in β the magnitude of the strongest reverse flow increases only slightly and moves against the basic flow direction to $(-1.4L_x, 0)$. For wide mountains upstream propagating columnar modes occur with the onset of wave breaking. Exceeding the breaking threshold, therefore, produces an additional source for a speed decrease ahead of the barrier. When the blocking threshold is reached, the strength of the reverse flow grows only slightly. Moreover, no stationary state is attained at the end of the simulation, the reverse flow still increases slightly with time.

The deceleration downstream of the barrier is represented in Fig. 14c. For very small H_m the speed reduction due to a convergence of air behind the barrier is larger the smaller β since more air is diverted laterally around the barrier the smaller β (cf. Bauer 1997). For long mountains the location of the minimum approaches the mountain top with increasing H_m (e.g., for $\beta = 0.25$: $u_{\min}$ at $x = 6.6L_y$ for $H_m = 1.0$, at $x = 3.6L_y$ for $H_m = 2.0$, and at $x = 2.8L_y$ for $H_m = 3.0$). The air stagnates for the axisymmetric obstacle at lower mountain heights than for $\beta = 0.5$. Most obvious is the peak within the curve for $\beta = 1$ at $H_m = 1.25$. It is only a transient phenomenon of the flow. A snapshot is depicted in Fig.

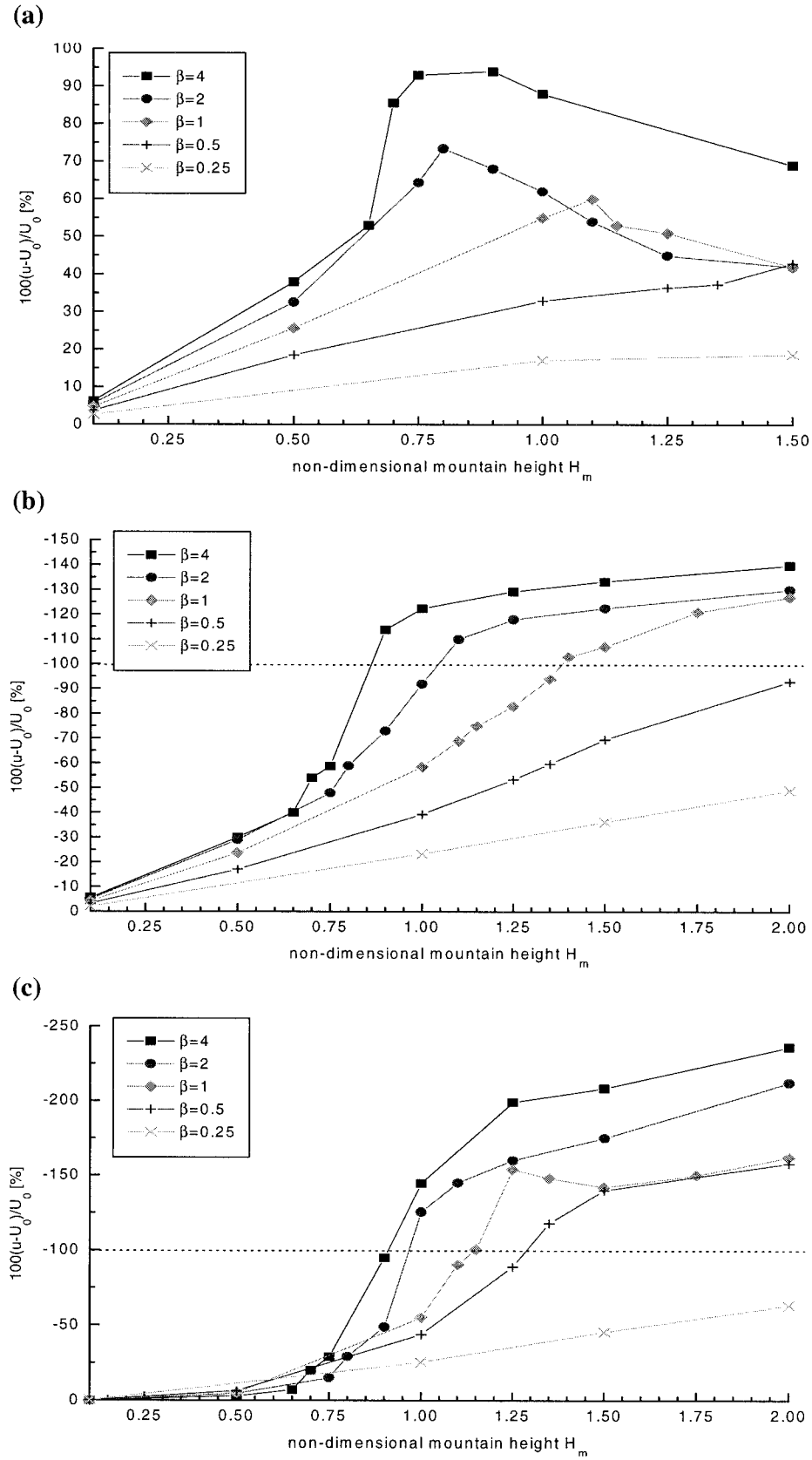

FIG. 14. Surface wind extrema: (a) maximum relative velocity surplus on the lee side, (b) maximum relative velocity reduction on the windward, and (c) on the leeward side in per cent as a function of H_m for various horizontal aspect ratios β. Dotted line indicates the threshold of stagnation.

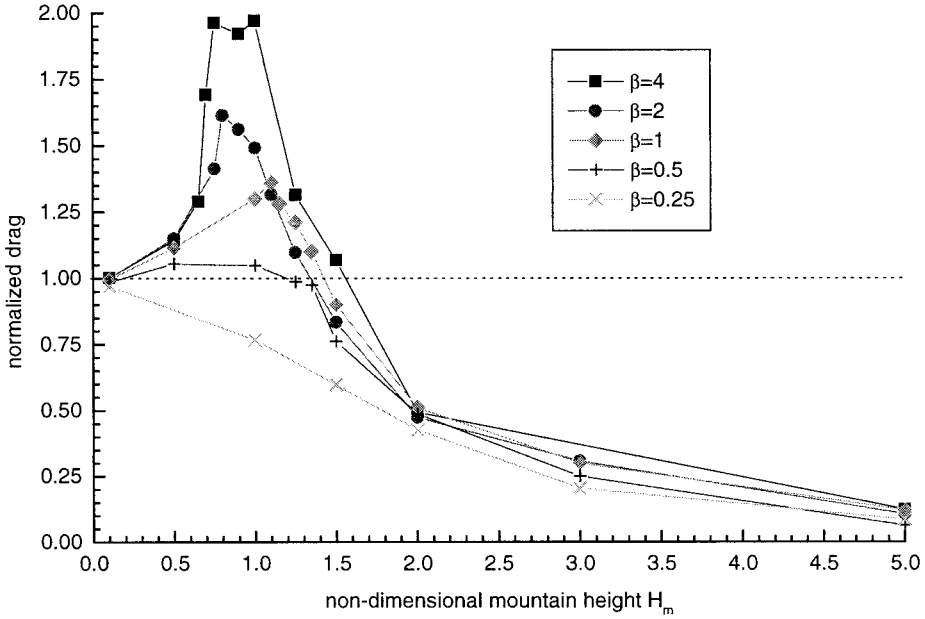

FIG. 15. Three-dimensional drag, normalized with the linear drag of a three-dimensional Gauss-mountain (see appendix) as a function of the nondimensional mountain height H_m for various horizontal aspect ratios β.

14 that is only valid at the simulation time chosen for the plot. Whereas for mountains with $H_m \geq 1.5$ lee vortices change only slightly after $T = 30$, the flow field for H_m close to 1.25 is still in a transition phase at that time. The negative momentum transport due to the turbulence zone, which is induced by wave breaking and expands downward, has reached the ground not long before the simulation stops and leads to an intensification of the reverse flow in the center of the vortices. With time this effect should diminish leading to a weaker leeward minimum and the elimination of the peak. For wide mountains wave breaking triggers the formation of a vortex pair at the surface. Therefore, the minimum increases almost jumplike when the downward propagating turbulent wake touches the ground. After the formation of these vortices the minimum moves downstream with time to about $(2L_y, 0)$, almost independently of H_m.

Figure 15 shows the three-dimensional drag normalized with its linear counterpart derived in the appendix. For $H_m \leq 0.1$ the drag closely matches the linear prediction. For $H_m = 0.5$ the effect of nonlinearity on the leeside velocity and pressure distribution leads to a drag surplus for large β. With the onset of wave breaking, high-drag states occur. The normalized drag is higher the larger β. But with the formation and continuous growth of lee vortices the normalized drag shows an almost equally strong decrease again. Even for large β it drops below its linear counterpart before $H_m = 2$ (cf. Olafsson and Bougeault 1996) and approaches zero asymptotically. Again, this is caused by the dampening effect of the reverse flow on the descent of potentially warmer air and on wave formation. The range of H_m where high-drag states appear becomes broader the larger β. Still, wide barriers are far from being quasi-two-dimensional. In this limiting case no lee vortices can exist and high-drag states appear for all H_m after the onset of wave breaking (e.g., Stein 1992). For long mountain ranges and large H_m the inability of the flow to climb the mountain top and the increasing horizontal deflection around the barrier entails drag values that are overestimated by linear theory.

4. Summary and conclusions

Within this article stream patterns were examined that were produced by flow impinging on a mesoscale Gaussian-shaped three-dimensional obstacle under free-slip nonrotational conditions. The fluid moves with a basic speed of $U = 10$ m s^{-1} in an initially continuously stratified atmosphere with a constant Brunt–Väisälä frequency of $N = 0.01$ s^{-1}. The following characteristics have been derived.

a. Weakly nonlinear range

Within the weakly nonlinear range where no stagnation points occur in the flow field, larger β means stronger vertical isentropic displacements, higher maximum wind speeds, and a stronger windward deceleration. This resembles the purely linear flow response (Blumen and Dietze 1981; Phillips 1984; Smith 1989a).

Barriers with $\beta > 1$ have a drag surplus due to the amplifying effect of nonlinearity on the leeward pressure and velocity field. In contrast, perturbations for mountain ranges with $\beta < 1$ produce a drag that is below the linear prediction. A more detailed discussion of this parameter range is given in Bauer (1997).

Linear theory predicts the possible occurrence of two stagnation points in the flow field: one upstream of the obstacle close to the surface and another one above the lee slope (Smith 1988). Nonlinear simulations indicate a third velocity minimum, which can become strong enough to produce a stagnation point and to form a counterrotating vortex pair.

b. Strongly nonlinear range

1) STAGNATION POINTS

Linear theory reveals that the *larger* β the *smaller* the critical H_m is for wave breaking and windward stagnation (Smith 1989a). This was confirmed by our nonlinear numerical simulations. Additionally, the same relation is true for lee vortex formation.

When stagnation occurs on the upstream side, a vortex with horizontal axis is formed (Smolarkiewicz and Rotunno 1990). With increasing H_m its separation point approaches the mountain top while the saddle point moves upstream; that is, the zone of windward stagnation spreads. The strength of the upstream reverse flow grows only slightly after the onset of blocking.

Lee vortices are forced by a violation of PV conservation (Smith 1989b; Schär and Durran 1997). For $\beta > 1$, PV is generated by wave breaking above the lee slope. Therefore, lee vortex formation is triggered by wave breaking for wide mountains. Without the wave breaking process the air along the lee slope would *not* stagnate at $H_m \sim 1$. For $\beta \leq 1$ the formation of a vortex pair is an independent process that is neither connected to wave breaking nor to wave overturning and flow splitting on the windward side. Both are, for example, absent for the demonstrated case of $\beta = 0.5$ and $H_m = 1.5$ (Fig. 12). For $\beta \leq 0.5$ lee vortices may exist although no wave breaking occurs for any H_m. For mountains with $\beta \leq 1$ the transition to lee stagnation near the surface is not jumplike but is indeed a consequence of the gradual velocity reduction due to the increasing (with H_m) horizontal confluence behind the obstacle. The dissipative process leading to PV anomalies is the overturning of isentropes and subsequent wave breaking locally at this stagnation point. It is the location where vortices are generated and from where they move slightly upstream and grow with time.

When stagnation occurs at the leeside surface it takes a time span $\Delta T \gg O(10)$ for the ensuing lee vortices to become stationary (Schär and Durran 1997). In a first phase they widen and move downstream. In a second phase they elongate considerably while the vortex center remains almost at the same location. For $\beta \geq 1$ the final location of the center of the leeside vortex pair is close to $2L_y$ downstream of the mountain top and almost independent of H_m.

2) VELOCITY

For $\beta \leq 1$ the air is continuously decelerated ahead of the barrier with increasing H_m due to the piling up of heavy air. The windward velocity distribution is not influenced by the leeside wave breaking event or by the formation of lee vortices. For $\beta > 1$ two distinct processes can reduce the flow speed upstream of a barrier: the before-mentioned blocking effect by the piling up of air and, secondly, the upstream propagation of columnar modes produced by wave breaking (Smolarkiewicz and Rotunno 1990). Still, for mountain ranges with $\beta \leq 4$ (and probably also for much larger β) the predominant deceleration effect comes from the blocking in front of the barrier.

The maximum wind speed increases considerably after the onset of wave breaking as long as there is *no* lee vortex formation. The magnitude of this ''downslope windstorm'' and the range of H_m where it occurs is larger when β is larger. When lee vortices are present, their growth (with time and with H_m) dampens the downslope descent of potentially warmer air and, thereby, reduces the maximum wind speed. For long mountains ($\beta < 1$) with high H_m the wind maximum does not occur along the leeward slope but at the lateral flanks slightly downstream of the crest.

3) DRAG

For all H_m the normalized drag is higher the larger β. Moreover, the range of H_m where ''high-drag'' states appear is broader the larger β. But wide barriers are still far from being quasi-two-dimensional, since in the two-dimensional case no lee vortices can form and high-drag states appear for *all* H_m after the onset of wave breaking (e.g., Stein 1992).

When regime boundaries are crossed, the ensuing wakes are at first very weak. For example, high drag states are only gradually dampened by the growth of lee vortices with increasing H_m. The transition from one flow regime to the other is therefore possibly too continuous to name it a bifurcation.

Acknowledgments. This work originated as part of a dissertation at the University of Innsbruck. The financial support by the ''Österreichischer Fond zur Förderung der Wissenschaftlichen Forschung—FWF'' through Project P-10278GEO (''Systematic investigation of flow over and around an obstacle with the inclusion of downslope winds'') is gratefully acknowledged.

APPENDIX

Linear Drag on a Gaussian Mountain with $L_x \neq L_y$

In the present simulations, flow along the x axis impinging upon an elliptical Gaussian-shaped mountain,

$$h(x, y) = h_m \exp\left[-\left(\frac{x}{L_x}\right)^2 - \left(\frac{y}{L_y}\right)^2\right], \quad \text{(A1)}$$

has been investigated. The Fourier transform of (A1),

$$\hat{h}(k, l) = \frac{h_m}{4\pi^2} \int_{-\infty}^{+\infty} \int_{-\infty}^{+\infty} \exp\left[-\left(\frac{x}{L_x}\right)^2\right] \exp\left[-\left(\frac{y}{L_y}\right)^2\right] e^{-ikx} e^{-ily}\, dx\, dy, \quad \text{(A2)}$$

where k and l are horizontal wavenumbers in the x and y directions, may be integrated to give

$$\hat{h}(k, l) = \frac{h_m}{4\pi} L_x L_y \exp\left(-\frac{k^2 L_x^2}{4} - \frac{l^2 L_y^2}{4}\right). \quad \text{(A3)}$$

Following Smith and Grønas (1993), the drag can be expressed as

$$D = 4\pi^2 \rho_0 N_0^2 \int_{-\infty}^{+\infty} \int_{-\infty}^{+\infty} \frac{k}{m} \hat{h}(k, l) \hat{h}^*(k, l)\, dk\, dl, \quad \text{(A4)}$$

where $\hat{h}^*$ is the complex conjugate of $\hat{h}$, and the index 0 denotes basic-state variables. The vertical wavenumber m in the classic gravity wave solution is given by

$$m = \frac{N_0 \sqrt{k^2 + l^2}}{U_0 k}. \quad \text{(A5)}$$

Using (A3) and (A5), Eq. (A4) becomes

$$D = 4\pi^2 \rho_0 N_0^2 \int_{-\infty}^{+\infty} \int_{-\infty}^{+\infty} \frac{U_0 k^2}{N_0 \sqrt{k^2 + l^2}} \frac{h_m^2}{(4\pi)^2} L_x^2 L_y^2 \exp\left(-\frac{k^2 L_x^2}{2} - \frac{l^2 L_y^2}{2}\right) dk\, dl. \quad \text{(A6)}$$

By transforming into polar coordinates

$$k = \kappa \cos\psi, \qquad l = \kappa \sin\psi, \quad \text{(A7)}$$

the linear drag of Eq. (A6) can be expressed as

$$D = C \rho_0 N_0 U_0 h_m^2 \sqrt{L_x L_y}\, I(\beta), \quad \text{(A8)}$$

where

$$C = (2\pi)^{3/2}/16 \quad \text{and} \quad \text{(A9)}$$

$$I(\beta) = \frac{1}{\pi} \int_0^{2\pi} \frac{\cos^2\psi\, d\psi}{\left(\frac{1}{\beta}\cos^2\psi + \beta \sin^2\psi\right)^{3/2}} \quad \text{(A10)}$$

using the horizontal aspect ratio $\beta = L_y/L_x$. Here, $I(\beta)$ can be related to an elliptical integral of the first kind. However, it is less tedious to perform the integration numerically. For $\beta = 1$, (A8) simplifies to the expression derived by Smith and Grønas (1993) for an axisymmetric mountain

$$D = C \rho_0 N_0 U_0 L h_m^2 \quad \text{(A11)}$$

since $I(1)$ equals 1. Integrating (A10) for the aspect ratios used in the simulations leads to values of I shown in Table A1. Inserting $I(\beta)$ into (A8), for example, reveals that by leaving L_y constant but stretching the barrier streamwise by a factor of 4 (i.e., $\beta = 0.25$) the drag is *lowered* by about 41%, while a streamwise compression by a factor of 4 (i.e., $\beta = 4$) *increases* the drag by 22%.

TABLE A1. Values of I as a function of β.

β	4	2	1	0.5	0.25
$I(\beta)$	2.436	1.613	1	0.567	0.293

REFERENCES

Bauer, M. H., 1997: Three-dimensional numerical simulations of the influence of the horizontal aspect ratio on flow over and around a meso-scale mountain. Ph.D. dissertation, University of Innsbruck, 334 pp. [Available from Department of Meteorology, University of Innsbruck, Innrain 52, 6020 Innsbruck, Austria.]

Blumen, W., and S. C. Dietze, 1981: An analysis of three-dimensional mountain lee waves in a stratified shear flow. *J. Atmos. Sci.,* **38,** 1949–1963.

Castro, I. P., 1987: A note on lee wave structures in stratified flow over three-dimensional obstacles. *Tellus,* **39A,** 72–81.

——, and W. H. Snyder, 1993: Experiments on wave breaking in stratified flow over obstacles. *J. Fluid Mech.,* **255,** 195–211.

Drazin, P. G., 1961: On the steady flow of a fluid of variable density past an obstacle. *Tellus,* **13,** 239–251.

Gal-Chen, T., and R. C. J. Somerville, 1975a: On the use of a co-

ordinate transformation for the solution of the Navier–Stokes equations. *J. Comput. Phys.,* **17,** 209–228.
——, and ——, 1975b: Numerical solution of the Navier-Stokes equations with topography. *J. Comput. Phys.,* **17,** 276–310.
Garner, S. T., 1995: Permanent and transient upstream effects in nonlinear stratified flow over a ridge. *J. Atmos. Sci.,* **52,** 227–246.
Georgelin, M., 1997: Simulation of the foehn-case of 12 January 1996: Unstationarity of the wave breaking area. *MAP Newsl.,* **7,** 62–63.
Grubišić, V., and P. K. Smolarkiewicz, 1997: The effect of critical levels on 3D orographic flows: Linear regime. *J. Atmos. Sci.,* **54,** 1943–1960.
——, R. B. Smith, and C. Schär, 1995: The effect of bottom friction on shallow-water flow past an isolated obstacle. *J. Atmos. Sci.,* **52,** 1985–2005.
Helfand, H. M., and J. C. Labraga, 1988: Design of a nonsingular level 2.5 second-order closure model for the prediction of atmospheric turbulence. *J. Atmos. Sci.,* **45,** 113–132.
Klemp, J. B., and R. B. Wilhelmson, 1978: The simulation of three-dimensional convective storm dynamics. *J. Atmos. Sci.,* **35,** 1070–1096.
Lyra, G., 1940: Über den Einfluß von Bodenerhebungen auf die Strömung einer stabil geschichteten Atmosphäre. *Beitr. Phys. Frei. Atmos.,* **26,** 197–206.
——, 1943: Theorie der stationären Leewellenströmung in freier Atmosphäre. *Z. Angew. Math. Mech.,* **23,** 1–28.
Mellor, G. L., and T. Yamada, 1982: Development of a turbulence closure model for geophysical fluid problems. *Rev. Geophys. Space Phys.,* **20,** 851–875.
Miranda, P. M. A., and I. N. James, 1992: Non-linear three-dimensional effects on gravity-wave drag: Splitting flow and breaking waves. *Quart. J. Roy. Meteor. Soc.,* **118,** 1057–1081.
——, and M. A. Valente, 1997: Critical level resonance in three-dimensional flow past isolated mountains. *J. Atmos. Sci.,* **54,** 1574–1588.
Olafsson, H., 1996: *Atlas des écoulements hydrostatiques autour d'un relief idéalisé.* Centre National de Recherches Météorologiques Tech. Rep. 42, 86 pp. [Available from CNRM, 42 Av. Coriolis, 31057 Toulouse, France.]
——, and P. Bougeault, 1996: Nonlinear flow past an elliptic mountain ridge. *J. Atmos. Sci.,* **53,** 2465–2489.
——, and ——, 1997: The effect of rotation and surface friction on orographic drag. *J. Atmos. Sci.,* **54,** 193–210.
Peng, M. S., S.-W. Li, S. W. Chang, and R. T. Williams, 1995: Flow over mountains: Coriolis force, transient troughs and three dimensionality. *Quart. J. Roy. Meteor. Soc.,* **121,** 593–613.
Phillips, D. S., 1984: Analytical surface pressure and drag for linear hydrostatic flow over three-dimensional elliptical mountains. *J. Atmos. Sci.,* **41,** 1073–1084.
Pielke, R. A., and Coauthors, 1992: A comprehensive meteorological modeling system—RAMS. *Meteor. Atmos. Phys.,* **49,** 69–91.
Pierrehumbert, R. T., and B. Wyman, 1985: Upstream effects of mesoscale mountains. *J. Atmos. Sci.,* **42,** 977–1003.
Queney, P., 1948: The problem of airflow over mountains: A summary of theoretical studies. *Bull. Amer. Meteor. Soc.,* **29,** 16–26.
Schär, C., and D. R. Durran, 1997: Vortex formation and vortex shedding in continuously stratified flows past isolated topography. *J. Atmos. Sci.,* **54,** 534–554.
Scorer, R. S., 1956: Airflow over an isolated hill. *Quart. J. Roy. Meteor. Soc.,* **82,** 75–81.
Shutts, G. J., 1998: Stationary gravity-wave structure in flows with directional wind shear. *Quart. J. Roy. Meteor. Soc.,* **124,** 1421–1442.
Smagorinsky, J., 1963: General circulation experiments with the primitive equations: I. The basic experiments. *Mon. Wea. Rev.,* **91,** 99–164.
Smith, R. B., 1980: Linear theory of stratified hydrostatic flow past an isolated mountain. *Tellus,* **32,** 348–364.
——, 1982: Synoptic observations and theory of orographically disturbed wind and pressure. *J. Atmos. Sci.,* **39,** 60–70.
——, 1988: Linear theory of stratified flow past an isolated mountain in isosteric coordinates. *J. Atmos. Sci.,* **45,** 3889–3896.
——, 1989a: Mountain-induced stagnation points in hydrostatic flow. *Tellus,* **41A,** 270–274.
——, 1989b: Comment on ''Low Froude number flow past three-dimensional obstacles. Part I: Baroclinically generated lee vortices.'' *J. Atmos. Sci.,* **46,** 3611–3613.
——, and S. Grønas, 1993: Stagnation points and bifurcation in 3-D mountain airflow. *Tellus,* **45A,** 28–43.
Smolarkiewicz, P. K., and R. Rotunno, 1989: Low Froude number flow past three-dimensional obstacles. Part I: Baroclinically generated lee vortices. *J. Atmos. Sci.,* **46,** 1154–1164.
——, and ——, 1990: Low Froude number flow past three-dimensional obstacles. Part II: Upwind flow reversal zone. *J. Atmos. Sci.,* **47,** 1498–1511.
Stein, J., 1992: Investigation of the regime diagram of hydrostatic flow over a mountain with a primitive equation model. Part I: Two-dimensional flows. *Mon. Wea. Rev.,* **120,** 2962–2976.
Sun, W.-Y., and J.-D. Chern, 1994: Numerical experiments of vortices in the wakes of large idealized mountains. *J. Atmos. Sci.,* **51,** 191–209.
Thorsteinsson, S., 1988: Finite amplitude stratified air flow past isolated mountains on an f-plane. *Tellus,* **40A,** 220–236.
——, and S. Sigurdsson, 1996: Orogenic blocking and deflection of stratified air flow on an f-plane. *Tellus,* **48A,** 572–583.
Trüb, J., 1993: Dynamical aspects of flow over alpine-scale orography: A modeling perspective. Ph.D. dissertation, Swiss Federal Institute of Technology Zürich, 140 pp. [Available from Institute for Atmospheric Science, Swiss Federal Institute of Technology, ETH Hönggerberg, CH-8093 Zurich, Switzerland.]
Wolyn, P. G., and T. B. McKee, 1992: Modeling and observational study of the daytime evolution east of the crest of the Colorado Rockies. Climatology Rep. 92-1, Dept. of Atmospheric Science, Colorado State University, Fort Collins, CO, 255 pp. [Available from Department of Atmospheric Science, Colorado State University, Fort Collins, CO 80523.]